Smart Structures and Systems, *Vol. 23, No. 4 (2019) 319-327*
DOI: https://doi.org/10.12989/sss.2019.23.4.319

A harmonic movable tooth drive system integrated with shape memory alloys

Lizhong Xu*, Zongxing Cai and Xiaodong He

Department of Mechanical Engineering, Yanshan University,
Hebei street 438, Qinhuangdao, 066004, People's Republic of China

(Received April 21, 2016, Revised March 9, 2019, Accepted March 12, 2019)

Abstract. Continuous rotating SMA actuators require motion conversion mechanisms, so their structure is relatively complex and difficult to realize the miniaturization. Here, a new type of continuous rotating actuator driven by SMA is proposed. It combines the movable tooth drive with SMA drive. The structure and working principle of the integrated movable tooth drive system is introduced. The equations of temperature, stress and strain of memory alloy wires, and the output torque of drive system are given. Using these equations, the temperature, the output forces of the SMA wires, and output torque of the drive system are studied. Results show that the compact drive system could give large output torque. To obtain large output torque plus small fluctuation, large eccentricity and small diameter of the SMA wire should be taken. Combined application of ventilation cooling and high current can increase the rotary speed of the drive system.

Keywords: shape memory alloys; movable tooth drive; integrated; output torque; driving force

1. Introduction

Shape memory alloy (SMA) has the advantages of high power density, high recovery strain, clean and silent, low working voltage and simple structure (Hugo 2016, Lee 2015). These advantages make SMA very suitable for low-speed, compact, large-load actuators. Actuators based on shape memory effect have been widely used in aerospace, robotics, biomedical engineering and automotive engineering (Wang 2008, Laschi 2009, Potnuu 2015, Tanaka 1991). SMA actuators include two types: linear motion actuators and rotary motion actuators. Linear motion actuators are simple because they work directly using the linear shrinkage deformation of SMA. The rotating actuator needs to transform the linear shrinkage deformation of SMA into rotational motion.

Tanaka (1991) developed a SMA rotary actuator that placed two SMA conductors with pulleys oppositely in which, the center shaft achieved bidirectional rotation in a limited range of angles. By winding the SMA wire over a set of pulleys, Song (2007) increased the effective length of the SMA wire and the rotation angle range of actuator. Carpenter (1995) proposed a rotating actuator using SMA helical spring, in which the NiTiCu alloy wire is wound in the helical spring actuator, and the universal joint rotation is controlled by mechanical elements. The linear motion of the antagonistic SMA spring is transformed into rotational motion. At a rotational speed of 0.060/s, the universal joint can be rotated between -100^0 and 100^0, with a maximum output torque of 0.34 Nm. Based on torsional deformation of torsional SMA elements, Gabriel (1988), Tobushi (2011) designed micro SMA rotary actuators. Yuan (2018) proposed a rotating actuator driven by SMA wires in 3D printing helical structure, which realized the complete reversible rotation of 150 degrees.

The characteristic of the SMA rotary actuators above is that the structure is relatively simple, but it could not be rotated continuously. Some continuous rotating SMA actuators have also been proposed and studied. Using SMA bending spring, Warith (1998) manufactured a continuous rotation servo motor. However, the energy density in the bending mode is much smaller than that in the contraction mode. Therefore, the output torque is very small. Gorbet (1995) proposed a differential continuous rotating SMA actuator with two SMA wires. Lan (2009) investigated a continuous rotary actuator using the bending mechanism of the SMA wire, in which the SMA wire is used as the driver and the bending mechanism acts as a load transmitter. Yan (2012) developed a kind of continuous rotating motor driven by five shape memory alloy wires. Five rotating actuators were fixed on a single shaft in series to realize the one-way continuous rotation of the output shaft with a rotational speed of 0.28 r / min. The harmonic gear drive driven by SMA line is put forward by Meier (2004). Here, the meshing between rigid gear and flexible ring is controlled by SMA wires, and the reduction ratio is realized. Hwang (2014, 2016) combined with the principle of the SMA actuator and the swing step motor, proposed a continuous rotating SMA actuator in which the inner ring is driven by the contraction force of the SMA wire, and the inner ring meshes with the outer gear teeth, thus the output shaft is driven to rotate continuously.

In short, a great deal of research has been done on SMA actuators. However, continuous rotating SMA actuators require motion conversion mechanisms, so their structure is

*Corresponding author, Professor
E-mail: xlz@ysu.edu.cn

http://www.techno-press.com/journals/sss&subpage=7
ISSN: 1738-1584 (Print), 1738-1991 (Online)

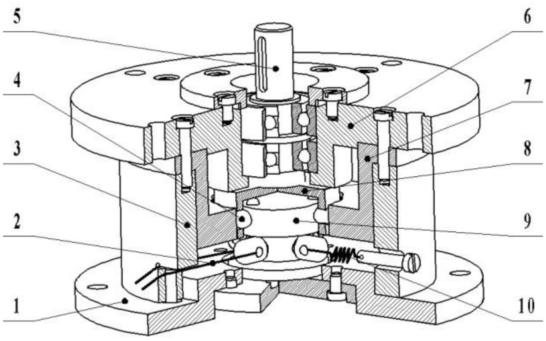

Fig. 1 A harmonic movable tooth drive system integrated with shape memory alloys. 1. base; 2. SMA wire; .3 housing; 4. movable teeth; 5. output shaft; 6. upper end cover; 7. center wheel; 8. movable tooth rack; 9. wave generator; 10. offset spring

relatively complex, and difficult to realize the miniaturization.

In this paper, a new type of continuous rotating actuator driven by SMA is proposed. It combines movable tooth drive with SMA drive. It is simple structure and easy to achieve miniaturization. This paper introduces the structure and working principle of the integrated harmonic movable tooth drive system. The calculation equations of temperature, stress and strain of memory alloy wires, and the output torque of drive system are given. Using these equations, the temperature, output forces of the memory alloy wires, and output torque of the drive system are studied. The results show that the drive system can achieve relatively large output torque with a compact structure

2. Design

The structure of harmonic movable tooth drive system integrated with shape memory alloys is shown in Fig. 1. The drive system includes the SMA driving part and the movable tooth transmission part: the SMA driving part is composed of two groups of SMA wires and the corresponding offset springs. The transmission part is a movable tooth transmission system, which is composed of movable tooth, center wheel, movable tooth rack and wave generator. The center wheel is fixed on the outer shell, and the movable tooth rack is fixed to the output shaft.

The working principle of the electromechanical integrated SMA harmonic drive system is as follows:

At the beginning of the work, the square wave current of 1:1 duty cycle ratio is applied to the SMA wire to one side (set as the direction I). When the SMA wire is heated by the current, the temperature of the SMA wire with martensite is gone up, and the transformation from martensite to austenite occurs (martensite is changed into austenite), the stress in the SMA wire increases, the length of the SMA wire shrinks, driving the wave generator motion. When the current becomes zero, the SMA wire is still in austenitic state, and transformation from austenite to martensite occurs (austenite is changed into martensite), the stress in the SMA wire decreases, and the corresponding bias spring draws the SMA wire (resulting in plastic deformation) and drives the wave generator motion. Thus, the wave generator forms reciprocating motion during the heating and cooling of the SMA wire. At the same time, the square wave current with the same frequency, the same amplitude of square wave current is applied to the other side (set as the direction II) of the SMA wires with delay of 1/4 period. Therefore, the reciprocating motion of the wave generator in the two orthogonal directions superposes to form a traveling wave, that is, the center of the wave generator forms a circular track of rotation around the fixed center, which pushes the movable teeth and makes the output shaft fixed with the movable tooth frame to rotate continuously and output torque.

3. Temperature in SMA wire

In cylindrical coordinate system, the heat conduction differential equation of SMA wire is

$$V\left[\frac{1}{r}\frac{\partial}{\partial r}\left(\lambda_1 r\frac{\partial T}{\partial r}\right)+\frac{1}{r^2}\frac{\partial}{\partial\theta}\left(\lambda_1\frac{\partial T}{\partial\theta}\right)+\frac{\partial}{\partial z}\left(\lambda_1\frac{\partial T}{\partial z}\right)\right]+\frac{dq}{dt}=\frac{dE}{dt} \tag{1}$$

where dq/dt is heat exchange rate between SMA wire and air (W·m^{-2}·°**C**$^{-1}$); dE/dt is change rate of storage energy of SMA wire (W·m^{-2}·°**C**$^{-1}$); T is temperature of SMA wire(°C); λ_1 is thermal conductivity of SMA wire (W·m^{-1}·°**C**$^{-1}$); r is radial coordinate; z is axial coordinate, θ is angle coordinate.

In order to solve the heat conduction differential equation of SMA wire, the following simplifications and assumptions are made:

(1) Since the length (20 mm) of the SMA wire used here is much larger than its diameter (0.3-0.5 mm), the temperature change in the length direction of the SMA wire can be ignored;

(2) Assuming that the ambient temperature is uniform, the SMA wire does not have heat exchange in the tangent direction;

(3) According to the heat conduction theory, the temperature of the SMA wire in the radial direction is considered to be the same when the Bi-O number is less than 0.1. The expression of the Bi-O number is: $B_i = hr_0/2\lambda_1$, here h is the convective heat transfer coefficient of the SMA wire and air; r_0 the radius of the SMA wire. The convective heat transfer coefficient can be calculated by

$$h=\left\{0.6+\frac{0.387\left[gU(T-T_0)d_0^3\right]^{1/6}}{(D_T\nu)^{1/6}\left[1+(0.559/p_r)^{9/16}\right]^{8/27}}\right\}^2\frac{\lambda_0}{d_0} \tag{2}$$

where U is thermal expansion coefficient of air; T_0 is initial temperature (°**C**); D_T is thermal diffusion coefficient of air; ν is viscosity coefficient of air; p_r is Prandtl number of air; d_0 is average diameter of SMA wire (mm); g is acceleration of gravity (m·s^{-2}).

For the SMA wire here, the convection heat transfer coefficient is obtained from Eq. (2), h=5W/m^{2}K; Thus, the Bi-O number is $B_i = 4.028\times10^{-4} << 0.1$. So, the differential equation of heat conduction of SMA Wire can be simplified to

$$\frac{dq}{dt} = \frac{dE}{dt} \tag{3}$$

The heat exchange rate between SMA wire and air is closely related to the heating and cooling mode of SMA wire. The constant current heating and air cooling are taken as an example. During heating, the heat exchange rate between SMA wire and air is as follows

$$\frac{dq}{dt} = I^2R - hA_{surf}(T - T_0) \tag{4}$$

where I is heating current (A); R is average Resistance of SMA Wire (Ω); A_{surf} is surface area of SMA wire(m^2).

During cooling, the heat transfer rate between SMA wire and air is as follows

$$\frac{dq}{dt} = -hA_{surf}(T - T_0) \tag{5}$$

In the integrated SMA harmonic drive system, the change of storage energy of SMA wire is realized by increasing the temperature and absorbing the latent heat of phase transition. When SMA is in the non-phase transition region, change of storage energy of SMA wire is

$$\frac{dE}{dt} = mC_p\frac{dT}{dt} \tag{6}$$

where m is mass of SMA wire(kg); C_p is constant-pressure specific heat (J·kg^{-1o}C^{-1}).

When SMA is in the phase transition region, change of storage energy of SMA wire is

$$\frac{dE}{dt} = mC_p\frac{dT}{dt} - mQ_i\frac{d\xi}{dt} \tag{7}$$

where Q_i is phase change latent heat (J·kg^{-1}).

The change rate of martensite content ξ to time is as follows

$$\frac{d\xi}{dt} = \frac{d\xi}{dT}\frac{dT}{dt} + \frac{d\xi}{d\sigma}\frac{d\sigma}{dt} \tag{8}$$

Combining Eq. (3) with (4)-(8), the heat conductivity differential equation of SMA wire in heating process can be given as

$$\begin{aligned} & mC_p\frac{dT}{dt} + mQ_i\cdot\frac{a_A}{2}\cdot\sin\left[a_A\left(T - A_s - \frac{\sigma}{C_A}\right)\right]\cdot\frac{dT}{dt} \\ & - mQ_i\cdot\frac{a_A}{2C_A}\cdot\sin\left[a_A\left(T - A_s - \frac{\sigma}{C_A}\right)\right]\cdot\frac{d\sigma}{dt} \\ & = I^2R - hA_{surf}(T - T_0) \end{aligned} \tag{9}$$

In a same manner, differential equation of heat conduction of SMA wire in cooling process is

$$\begin{aligned} & mC_p\frac{dT}{dt} + mQ_i\cdot\frac{a_M}{2}\cdot\sin\left[a_M\left(T - M_f - \frac{\sigma}{C_M}\right)\right]\cdot\frac{dT}{dt} \\ & - mQ_i\cdot\frac{a_M}{2C_M}\cdot\sin\left[a_M\left(T - M_f - \frac{\sigma}{C_M}\right)\right]\cdot\frac{d\sigma}{dt} \\ & = -hA_{surf}(T - T_0) \end{aligned} \tag{10}$$

Because the mass and surface area of SMA wire are small and the heat produced by current heating is much larger than that of phase change latent heat and radiation heat transfer, the heat effect equation of SMA wire in driving part can be simplified. The heat conductivity differential equation of SMA wire in heating process can be simplified as

$$mC_p\frac{dT}{dt} = I^2R - hA_{surf}(T - T_0) \tag{11}$$

In Eq. (11), the current I is taken to be zero, it is just changed into the differential equation of heat conduction of SMA wire in cooling process .

4. Stress and strain of SMA wires

Transformation energy $f(\xi^t, \xi^d)$ related to inverse martensite transformation process is

$$f(\xi^t, \xi^d) = \left[a_d\left(1 - sgn\dot{\xi}^d\right) + b_d\left(1 + sgn\dot{\xi}^d\right)\right]\cdot\left[\frac{(\xi^d)^2}{4} + \frac{(\xi^d - 1/2)^4}{2} + \frac{\xi^d}{4}\right] \tag{12}$$

where ξ^d is stress induced martensite content (%); a_d , b_d are constitutive model parameters during inverse martensite transformation process

$$\begin{cases} a_d = \dfrac{\frac{1}{2}\Delta E(\varepsilon_{Af}^2 - \varepsilon_{As}^2) + (\sigma_{As} - \sigma_{Af})\varepsilon_{\max}}{2} \\ b_d = \dfrac{\frac{1}{2}\Delta E(\varepsilon_{Ms}^2 - \varepsilon_{Mf}^2) + (\sigma_{Mf} - \sigma_{Ms})\varepsilon_{\max}}{2} \end{cases}$$

Here $\varepsilon_{\max}$ is the maximum phase transformation strain (%); ΔE is variation of elastic modulus (MPa), $\Delta E = E(\xi) - E_M$, E_M is elastic modulus of martensite (MPa); σ_{As} , σ_{Af} , σ_{Ms} and σ_{Mf} are critical stress at the beginning and end of austenite and martensite Transformation in SMA, respectively:

$$\begin{cases} \sigma_{As} = (T_0 - A_s)C_A \ , \quad \sigma_{Af} = (T_0 - A_f)C_A \\ \sigma_{Ms} = \sigma_s + (T_0 - M_s)C_M \ , \ \sigma_{Mf} = \sigma_f + (T_0 - M_s)C_M \end{cases}$$

M_s is temperature at the beginning of martensitic transformation (^{o}C); M_f is temperature at the end of martensitic transformation (^{o}C); C_M is effect coefficient of martensitic transformation stress (MPa·^{o}C^{-1}); A_f is temperature at the end of austenitic transformation (°C); A_s is temperature at which austenitic transformation begins (°C); C_A is influence coefficient of austenitic transformation stress (MPa·°C^{-1}).

ε_{As}, ε_{Af}, ε_{Ms} and ε_{Mf} are elastic strains corresponding to σ_{As}, σ_{Af}, σ_{Ms} and σ_{Mf}:

$$\begin{cases} \varepsilon_{As} = \varepsilon_{\max} + \dfrac{\sigma_{As}}{E_M}, & \varepsilon_{Af} = \varepsilon_{\max} + \dfrac{\sigma_{Af}}{E_A} \\ \varepsilon_{Ms} = \dfrac{\sigma_{Ms}}{E_M}, & \varepsilon_{Mf} = \dfrac{\sigma_{Mf}}{E_M} \end{cases}$$

$sgn(x)$ is sign function:

$$\operatorname{sgn}(x) = \begin{cases} 1, & x > 0 \\ 0, & x = 0 \\ -1, & x < 0 \end{cases}$$

The total content ξ of martensite in the process of inverse martensite transformation is

$$\xi = \frac{\xi_0}{2}\left\{\cos\left[a_A\left(T - A_s - \frac{\sigma}{C_A}\right)\right] + 1\right\} \tag{13}$$

where ξ_0 is content of martensite in initial state (%); a_A is parameter related to austenitic transformation temperature, $a_A = \pi / (A_f - A_s)$.

Stress induced martensite content ξ^d is

$$\xi^d = \xi_0^d - \frac{\xi_0^d}{\xi_0}(\xi_0 - \xi) \tag{14}$$

where ξ_0^d is martensite content induced by initial state stress (%).

Temperature-induced martensite content ξ^t is

$$\xi^t = \xi_0^t - \frac{\xi_0^t}{\xi_0}(\xi_0 - \xi) \tag{15}$$

where ξ_0^t is martensite content induced by initial state temperature (%).

Martensite inverse transformation function F^{d2} is

$$F^{d2} = -X^d - R^{d2} \tag{16}$$

where X^d is phase change driving force; R^{d2} is critical value of phase change driving force.

Driving force X^d of phase transformation during inverse transformation of martensite is

$$X^d = -\rho\frac{\partial\psi}{\partial\xi^d} = -\left[\frac{1}{2}\Delta E(\varepsilon - \varepsilon^t)^2 - \sigma\varepsilon_{\max} + \rho(\Delta u_0 - \Delta\eta_0 T) + \frac{df}{d\xi^d}\right] \tag{17}$$

where ψ is free energy of SMA; ε^t is phase transformation strain; ρ is density of SMA wire (kg·m^{-3}); Δu_0 is changes in internal energy (J·kg^{-1}·°C^{-1}); $\Delta\eta_0$ is entropy change (J·kg^{-1}·°C^{-1}).

The critical value R^{d2} of phase transformation driving force in the process of inverse martensite transformation is as follows

$$R^{d2} = -\frac{1}{2}\Delta E\varepsilon_{Af}^2 - \rho(\Delta u_0 - \Delta\eta_0 T_0) + \sigma_{Af}\varepsilon_{\max} \tag{18}$$

The condition for the occurrence of inverse martensite transformation is $F^{d2}=0$. Thus, from Eqs. (16)-(18), we can give

$$\begin{aligned} &\frac{1}{2}\Delta E\left[(\varepsilon - \xi^d\varepsilon_{\max})^2 + \varepsilon_{Af}^2\right] - (\sigma + \sigma_{Af})\varepsilon_{\max} + \rho[2\Delta u_0 - \Delta\eta_0(T + T_0)] \\ &+ a_d \cdot \left[\frac{(\xi^d)^2}{4} + \frac{(\xi^d - 1/2)^4}{2} + \frac{\xi^d}{4}\right] = 0 \end{aligned} \tag{19}$$

The stress-strain relationship of SMA is

$$\sigma = E(\varepsilon - \xi^d\varepsilon_{\max}) \tag{20}$$

Elastic modulus E in Eq. (20) is a function of martensite content ξ, it equals to

$$E(\xi) = \xi \cdot E_M + (1 - \xi) \cdot E_A$$

Here, E_A is elastic modulus of austenite (MPa).

From Eqs. (19) and (20), stress and strain in SMA wire during inverse Martensite transformation can be obtained.

In a same manner, stress and strain in SMA wire during Martensite transformation can be given by following equations

$$\begin{aligned} &\frac{1}{2}\Delta E\left[\varepsilon_{Ms}^2 - (\varepsilon - \xi^d\varepsilon_{\max})^2\right] + (\sigma - \sigma_{Ms})\varepsilon_{\max} + \rho\Delta\eta_0(T - T_0) \\ &- b_d \cdot \left[\frac{(\xi^d)^2}{4} + \frac{(\xi^d - 1/2)^4}{2} + \frac{\xi^d}{4}\right] = 0 \end{aligned} \tag{21}$$

$$\sigma = E(\varepsilon - \xi^d\varepsilon_{\max}) \tag{22}$$

where $\Delta E = E(\xi) - E_A$;

$$\xi^d = \frac{1 - \xi_0^d}{2}\cos\left\{\frac{\pi}{\sigma_s^{cr} - \sigma_f^{cr}}\left[\sigma - \sigma_f^{cr} - C_M(T - M_s)\right]\right\} + \frac{1 + \xi_0^d}{2}$$

σ_s^{cr}, σ_f^{cr} are material constants reflecting the phase transition behavior of SMA.

The stress and strain in SMA wire can be obtained by substituting the temperature obtained from the heat conduction differential equation in section 3 into the Eqs. (19)-(22).

5. Output torque

In the transmission system, the wave generator contacts the movable teeth, and the movable teeth drive the rotation of the output shaft attached to it through the movable tooth rack. In the course of transmission, the movable teeth are subjected to the forces from the movable teeth frame, wave generator and center wheel. Force analysis of the meshing movable tooth is shown Fig. 2.

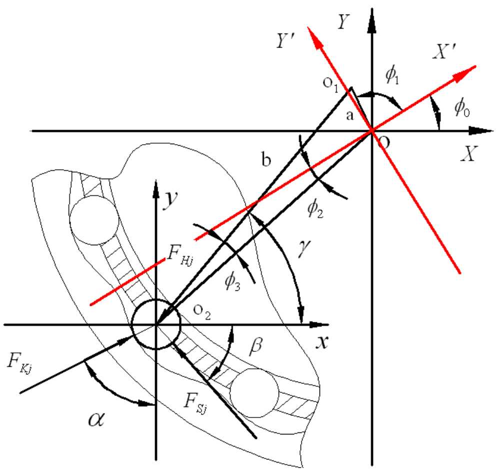

Fig. 2 Forces on the movable teeth

In Fig. 2, we know that $OO_1=a$ and $O_1O_2=R+r$. Here, a is eccentricity distance, R is radius of the wave generator, r is radius of movable tooth. Based on the sinusoidal theorem, we obtain

$$\phi_3 = \arcsin\left[a\sin(i-1)\phi_2/(R+r)\right] \tag{23}$$

where $i=\phi_1/\phi_2$, it is speed ratio of the system; ϕ_1 and ϕ_2 are rotation angle of the wave generator and output shaft, respectively.

The equation for the force balance of the j th movable teeth is

$$\left.\begin{aligned} F_{Kj}\sin\alpha - F_{Sj}\cos\beta - F_{Hj}\cos\gamma = 0 \\ F_{Kj}\cos\alpha + F_{Sj}\sin\beta - F_{Hj}\sin\gamma = 0 \end{aligned}\right\} \tag{24}$$

where F_{Kj} is normal force on movable teeth from central wheel (N); F_{Sj} is normal force on movable teeth from movable tooth rack (N); F_{Hj} is normal force on movable teeth from wave generator (N); n_b is tooth number of central wheel.

$$\left.\begin{aligned} &\alpha = \pi/2-\theta \\ &\beta = \pi/2-\gamma+\phi_3 \\ &\gamma = \phi_0+\phi_2+\phi_3 \\ &\phi_0 = \left[2\left(\lfloor (n_b+1)/2+1\rfloor - \lfloor (n_b+1)/2\rfloor\right)-1\right]\pi/n_b \end{aligned}\right\}$$

It is assumed that there is no clearance between the working parts, and a certain number of meshing movable teeth are in contact with the wave generator, resulting in elastic deformation at the contact point. The wave generator rotates a small angle and its elastic deformation ε_i is distributed according to the sine law. That is

$$\varepsilon_i = \left(\varepsilon\sin(n_b\phi_2)/\lambda\right)\sqrt{\lambda^2+1+2\lambda\cos\left[n_b\phi_2+\arcsin\left(\sin(n_b\phi_2)/\lambda\right)\right]} \tag{25}$$

where ε_i is elastic deformation of any movable tooth(mm); ε is the maximum elastic deformation of movable tooth (mm); $\lambda=(R+r)/a$.

If the force on movable tooth in mesh is approximately proportional to its deformation, then

$$F_{Hj} = \left(F_{j\max}\sin(n_b\phi_2)/\lambda\right)\sqrt{\lambda^2+1+2\lambda\cos\left[n_b\phi_2+\arcsin\left(\sin(n_b\phi_2)/\lambda\right)\right]} \tag{26}$$

where $F_{j\max}$ is the maximum force on movable tooth from wave generator.

From Eqs. (24) and (26), we can obtain

$$\left.\begin{aligned} F_{Sj} &= -F_{j\max}\sin(n_b\phi_2)\cos(\alpha+\gamma)\sqrt{\lambda^2+1+2\lambda\cos\left[n_b\phi_2+\arcsin\left(\sin(n_b\phi_2)/\lambda\right)\right]}\Big/\left[\lambda\cos(\alpha-\beta)\right] \\ F_{Kj} &= F_{j\max}\sin(n_b\phi_2)\sin(\beta+\gamma)\sqrt{\lambda^2+1+2\lambda\cos\left[n_b\phi_2+\arcsin\left(\sin(n_b\phi_2)/\lambda\right)\right]}\Big/\left[\lambda\cos(\alpha-\beta)\right] \end{aligned}\right\} \tag{27}$$

The output torque of the drive system can be calculated as

$$M = \sum_{j=1}^{n} F_{sj}S_c \tag{28}$$

where $S_c = aZ_{kj}$,

$$Z_{kj} = \sqrt{\lambda^2+1+2\lambda\cos\left\{n_b\phi_{2j}+\arcsin\left[\sin(n_b\phi_{2j})/\lambda\right]\right\}}$$

The output torque of the integrated system can be obtained by substituting the formula (27) into (28). One unknown parameter to be determined is the maximum force $F_{j\max}$ on the meshing teeth from wave generator.

Using the relation equation between maximum ball force and total radial force in rolling bearing, the relation equation between total force F and maximum movable tooth force $F_{j\max}$ from wave generator can be determined as follows.

$$F_{j\max} = \frac{F}{1+2\sum_{j=1}^{k} cos^{5/2}(j\varphi)} \tag{29}$$

where $F=\sqrt{F_x^2+F_y^2}$; $F_x = F_4 - F_2$ and $F_y = F_1 - F_3$. F_1 and F_2 are the tension forces in two-phase memory alloy wires, respectively, F_3 and F_4 are the forces in two springs; they are equal to:

$$\begin{cases} F_1 = \sigma_1\cdot A \\ F_2 = \sigma_2\cdot A \end{cases} \text{and} \quad \begin{cases} F_3 = k\cdot\Delta l_1 \\ F_4 = k\cdot\Delta l_2 \end{cases}$$

σ_1 and σ_2 are the stress in SMA wires, A is the section area of SMA wire; k is the stiffness of spring, Δl_1 and Δl_2 are the deformations of two SMA wires, respectively.

$$\begin{cases} \Delta l_1 = 2a+\dfrac{1}{2}\varepsilon_1\cdot l_0 \\ \Delta l_2 = 2a+\dfrac{1}{2}\varepsilon_2\cdot l_0 \end{cases}$$

Here, l_0 is the initial length of SMA wire, ε_1 and ε_2 are the strains of two SMA wires, respectively.

6. Results and discussion

The temperature rise and fall of memory alloy wire under the action of current pulse is calculated by using the temperature calculation formula given above, and it is found that the temperature increases rapidly under the action of current pulse. When the current pulse is removed, the temperature drops slowly. The cooling rate is much smaller than the heating rate. The memory alloy wire deformation produced by this law of temperature rise and fall could not realize the traveling wave motion required by harmonic movable tooth drive.

In order to realize the traveling wave motion of the wave generator, the cooling rate of the memory alloy wire should be equal to its heating rate. Therefore, two methods can be adopted: (1) adopting aeration-cooling to increase the cooling rate of memory alloy wires; (2) reducing the current, thus prolonging the heating time.

First, we adopt the second method to realize the condition that the cooling rate of the memory alloy wire is equal to the heating rate. Under this condition, the pulse heating current is 13.5 mA and the phase transition cycle is 4s. Thus, the cooling rate of memory alloy wire is basically equal to its heating rate (see Fig. 3). The basic parameters of memory alloy wire are shown in Table 1. Here, the surface convection heat transfer coefficient h=5w/ m^{2}K under natural conditions.

Changes of the resultant force F applied to the wave generator by the two-way memory alloy wires, the maximum radial force F_{jmax} applied to the movable tooth by the wave generator, and output torque M of the drive system are calculated (see Fig. 3) under the condition that the pulse current and the temperature changes are shown in Fig. 4. Parameters of the drive system used for calculation are given in Table 2. Fig. 4 shows:

(1). The driving force F produced by the SMA wires in the X-axis and the Y-axis direction is a periodic function with respect to the rotation angle of the wave generator, and the period is $\pi/2$. The maximum radial force F_{jmax} applied to the movable tooth by the wave generator is also periodically varied with a period of $\pi/2$. The periodic variation of the maximum radial force F_{jmax} and the output force F is due to the periodic expansion of the memory alloy wire. The shape memory alloy wire is in a periodic expansion process, wherein the tension is also periodically changed.

(2). In the drive system, the movable tooth drive the output shaft to rotate. Due to the periodic change of the force on the movable teeth, the output torque changes periodically. However, compared with the force fluctuation on the movable teeth, the fluctuation amplitude of the output torque is obviously reduced, which is due to the fact that the movable gear rack is driven by several movable teeth at the same time, so the overall fluctuation amplitude decreases.

By changing the system parameters, effects of the parameters on the performance of the system can be investigated. Fig. 5 shows the influence of the SMA wire diameter d and the eccentricity a of the wave generator on the driving force of the SMA wires and the output torque of the drive system. The influences of the parameters such as the radius of the movable tooth and the radius of the wave generator are relatively small and the corresponding calculated results are not given. Results show:

(1). The driving force F of the SMA wires and the output torque M of the drive system increase with the increase of the diameter d of the SMA wire, and the fluctuation amplitude increases significantly, but the relative fluctuation decreases with the increase of the diameter d of the SMA wire. As the diameter d of the SMA wire increases from 0.3 mm to 0.5 mm, the maximum driving force of the SMA wires increases from 3N to 8N, about 2.7 times, the fluctuation range increases from 1N to 2N, and the relative fluctuation decreases from 40% to about 30%. The maximum output torque of the drive system increases about 3.3 times from 10 Nmm to 33 Nmm, the fluctuation range increases from 2 Nmm to 4 Nmm, and the relative fluctuation decreases from 18% to about 12%. It can be seen that the diameter d of SMA wire has a significant effect on the driving performance of SMA wires and the output performance of the drive system.

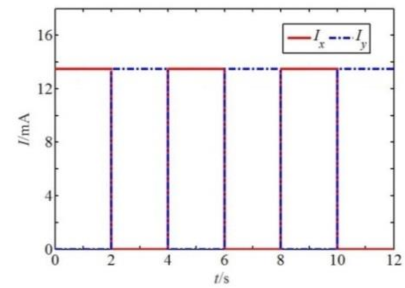

(a)

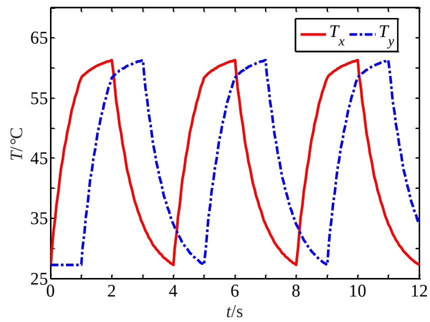

(b)

Fig. 3 (a) Pulse currents and (b) Temperature changes

Table 1 Parameters of the SMA wire

d mm	l_0 mm	ρ kg/m^3	s mm	σ_{af} MPa	σ_{as} MPa	σ_{Mf} MPa	σ_{Ms} MPa
0.3	20	6500	0.69	120	210	310	210
E_A MPa	E_M MPa	C_A MPa/^{0}C	C_M MPa/^{0}C	M_s ^{0}C	M_f ^{0}C	A_s ^{0}C	A_f ^{0}C
61500	24000	9	8	22	18	35	45
R_t Ω	C_p J/kgK	Δu_0 J/kgK	$\Delta \eta_0$ J/kgK	k N/mm	T_0 ^{0}C	Δh_M J/kg	Δh_A J/kg
0.08	30	-20	-17.8	8.65	25	11.2x10^{-3}	24.5x10^{-3}

Table 2 Parameters of the drive system

movable tooth number/n	ring tooth number/n_b	movable tooth radius/r	ave generator radius/R
15	14	1.5 mm	7.5 mm
eccentric center distance/a	outer radius of carrier/R_o	inner radius of carrier/R_i	speed ratio i
0.15 mm	10 mm	8.5 mm	15

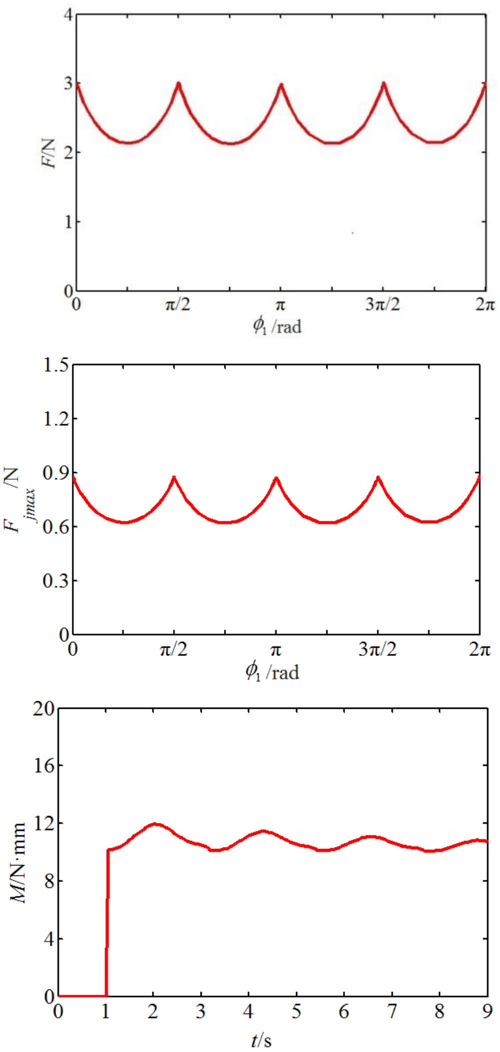

Fig. 4 Changes of the forces and torque in the drive system

(2) With the increase of the eccentricity of the wave generator, the driving force F of the SMA wires and the output torque M of the drive system increase, and the fluctuation amplitude increases obviously. When the eccentricity a increases from 0.2 mm to 0.4 mm, the maximum driving force of the SMA wires increases from 3N to 5.6N, about 1.9 times, and the fluctuation range increases from 1N to 1.9N. The relative fluctuation decreases from 40% to about 34%. The maximum output torque of the drive system increases by 2.8 times from 12 Nmm to 33 Nmm, the fluctuation range increases from 2 Nmm to 5 Nmm, and the relative fluctuation decreases from 17% to 15%. It can be seen that the eccentricity of the wave generator has a great influence on the driving performance of SMA wire and the output performance of the drive system. However, it has little effect on the relative fluctuation of wave generator and output torque.

(3) The influence of movable tooth radius and wave generator radius on force and output torque of the drive system is not significant, which can be negligible.

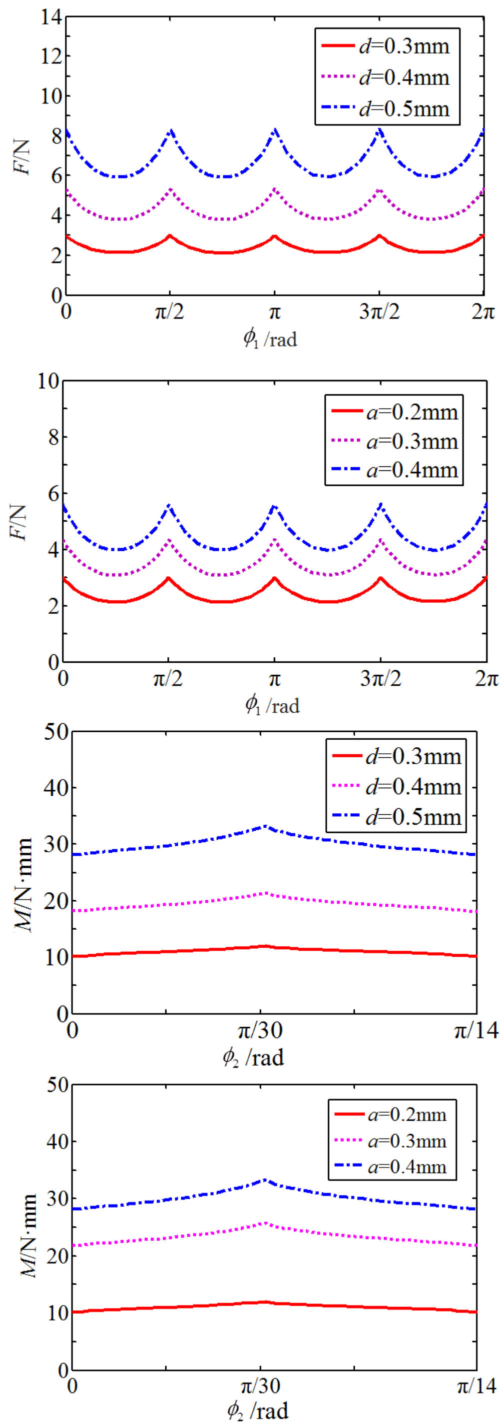

Fig. 5 Forces and output torque as function of a and d

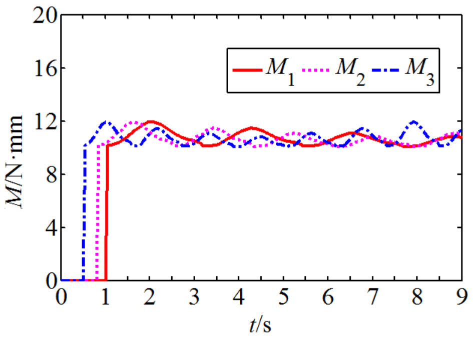

Fig. 6 Effects of input current on output torque

In conclusion, the output characteristic of the drive system is more sensitive to the diameter of the SMA wire and the eccentric distance of the wave generator. The output characteristics of the drive system are positively correlated with the diameter of the SMA wire and the eccentricity of the wave generator. No matter how the structural parameters change, the output performance of the drive system fluctuates with the angle of the output shaft, and the variation of the fluctuation amplitude is obvious. In order to obtain larger output torque and smaller absolute fluctuation values at the same time, the eccentricity and the diameter of the SMA wire should not be taken to be large values at the same time, and it is suggested to take the large eccentricity and the small diameter of the SMA wire.

Three different pulse currents are selected, and the input current in Y axis is 1 / 4 period behind X axis. The amplitudes of the pulse currents are 13.5 mA, 15.2 mA and 19.4mA, respectively. The periods of the current changes are 4s, 3.2s and 2s, respectively. The cooling modes are natural cooling (h=5 W/m^2·K), small air volume ventilation cooling (h=6.3 W/(m^2·K), and large air volume ventilation cooling (h=10.3 W/(m^2·K).

Three different input currents and corresponding cooling parameters are taken into account in the equations above-mentioned, and the influences of input current on the output characteristics of the drive system can be obtained (see Fig. 6). Fig. 6 shows:

When the input current is 1/ 4 period different on X axis and Y axis, with the increase of input current, the output torque of the drive system changes periodically with time, but the average value do not change with the input current. With the increase of the input current, the period of the output torque changes with time drops. The results show that the rotation speed of the output shaft is increased when the input current is increased.

The output torque of the drive system is independent of the current in the SMA wire, and its output speed is positively correlated with the current. The reason is that the wave generator swings one circle, which corresponds to the first cycle of the forward and inverse transformation of SMA wire martensite. The cycle time of forward and inverse martensite transformation in SMA wires is determined by the heating time and cooling time of SMA wire, and the cooling time is more important. The increasing of current amplitude can shorten the heating time of SMA wire, but it could not reduce the cooling time of SMA wire. The cooling time of SMA wire can be shortened by adopting large air volume ventilation cooling. Therefore, the combined application of ventilation cooling and high current can increase the rotary speed of the output shaft for the drive system.

In our drive system, only two SMA wires are used. The maximum output torque is about 11 Nmm which is four times more than that of Hwang's design (2014). In Hwang's design (2014), three SMA wires length in 50 mm are used and the maximum output torque is 2.5 Nmm. In our design, two SMA wires length in 20 mm are used. Thus, the output torque per unit length SMA wire is 11 Nmm/2x20 mm=0.275 Nmm/mm. In Hwang's design (2014), the output torque per unit length SMA wire is 2.5 Nmm/3x50 mm=0.017 Nmm/mm. It is about 1/16 of our drive system.

7. Conclusions

In this paper, a new type of continuous rotating actuator driven by SMA is proposed. It combines the principle of movable tooth drive and the principle of SMA drive. The structure and working principle of this kind of integrated harmonic movable tooth drive system is introduced. The equations of temperature, stress and strain of memory alloy wires, and the output torque of drive system are given. Using these equations, the temperature, the output forces of the memory alloy wires, and output torque of the drive system are studied. Results show:

- Relatively large output torque with a compact structure could be obtained with the drive system..
- The output characteristic of the drive system is more sensitive to the diameter of the SMA wire and the eccentric distance of the wave generator. In order to obtain larger output torque and smaller absolute wave values, larger eccentricity and smaller diameter of the SMA wire should be taken.
- The output torque of the drive system is independent of the current in the SMA wire, and its output speed is positively correlated with the current in the SMA wire. The combined application of ventilation cooling and high current can increase the rotary speed of the motor.

Acknowledgments

The research described in this paper was financially supported by the Natural Science Foundation of China.

References

André, I. and Eduardo, A. (2015), "A sliding mode torque and position controller for an antagonistic SMA actuator", *Mechatronics*, **30**,126-139.

Brinson, L. (1993), "One-dimensional constitutive behavior of shape memory alloys: thermo-mechanical derivation with non-constant material functions and redifined martensite internal variable", *J. Intel. Mat. Syst. Str.*, **4**(2), 229-242.

Carpenter, B., Head, J. and Gehling, R. (1995), "Shape memory

actuated gimbal", *Proc. SPIE*, **2447**, 90-101.
Gabriel, K., Trimmer, W. and Walker, J. (1988), "A micro rotary actuator using shape memory alloys", *Sens. Actuat*., **15**, 95-102.
Gorbet, R. and Russell, A. (1995), "A novel differential shape memory alloy actuator for position control", *Robotica.*, **13**(4), 423-430.
Hugo, R., Wei, W. and Hana, M. (2016), "Comparison of mold designs for SMA-based twisting soft actuator", *Sensor. Actuat. A: Phys.*, **237**, 96-106.
Hwang, D. and Higuchi, T. (2014), "A rotary actuator using shape memory alloy (SMA) wires", *IEEE/ASME T. Mechatron*., **19**(5), 1625-1635.
Hwang, D. and Higuchi, T. (2016), "A planar wobble motor with a XY Compliant mechanism driven by shape memory alloy", *IEEE/ASME T. Mechatron*., **21**(1), 302-315.
Huang, X.N., Kumar, K. and Jawed, M.K. (2018), "Chasing biomimetic locomotion speeds: Creating untethered soft robots with shape memory alloy actuators", *Science Robotics*., **3**(25), 7557.
Lee, H., Kim, S., Park, J., Kim, H. and Song, D. (2015), "Shape memory alloy (SMA)-based head and neck immobilizer for radiotherapy", *J. Comput. Des. Eng*., **2**, 176-182.
Laschi, C., Mazzolai, B., Mattoli, V., Cianchetti, M. and Dario, P. (2009), "Design of abiomimetic robotic octopus arm", *Bioinspir. Biomim*., **4**, 015006.
Lan, C., Wang, J. and Fan, C. (2009), "Optimal design of rotary manipulators using shape memory alloy wire actuated flexures", *Sensor. Actuat. A*., **153**(2), 258-266.
Meier, H. and Oelschlager, L. (2004), "Numerical modelling of the activation behaviour of SMA-actuator wires—Application in an innovative drive system", *Mat.-wiss. u. Werkstofftech*., **35**(5), 313-319.
Potnuru, A. and Tadesse, Y. (2015), "Artificial heart for humanoid robot using coiled SMA actuators", *Proceedings of SPIE - The International Society for Optical Engineering*., 9429, January, 2015, Bioinspiration, Biomimetics, and Bioreplication.
Song, G. (2007), "Design and control of a Nitinol wire actuated rotary servo", *Smart Mater. Struct*., **16**, 1796-1801.
Soriano-Heras, E., Blaya-Haro, F. and Molino, C. (2018), "Rapid prototyping prosthetic hand acting by a low-cost shape-memory-alloy actuator", *J. Artif. Organs*., **21**(2), 238-246.
Tanaka, Y. and Yamada, A. (1991), "A rotary actuator using shape memory alloy for a robot-analysis of the response with load", *IEEE/RSJ International Workshop on Intelligent Robots and Systems_91. Intelligence for Mechanical Systems*, IEEE., **2**,1163-1168.
Tobushi, H., Miyamoto, K., Nishimura, Y. and Mitsui, K. (2011), "Novel shape memory actuators", *J. Theory Appl. Mech*., **49**(3), 927-943.
Warith, M., Kennedy, K., Reitsma, R., Reynaerts, D. and Brussel, H. (1998), "Design aspects of shape memory actuators", *Mechatronics*., **8**(6), 635-656.
Yan, X., and Zhang, X. (2015), "Smart structures using shape memory alloy", Scientific press, Beijing, China.
Yuan, H., Chapelle, F., Fauroux, J.C. and Balandraud, X. (2018), "Concept for a 3D-printed soft rotary actuator driven by a shape-memory alloy", *Smart Mater. Struct*., **27**(5), 055005.
Zhang, X. and Yan, X. (2012), "Continuous rotary motor actuated by multiple segments of shape memory alloy wires", *J. Mater. Eng. Perform*., **21**(12), 2643-2649.

HJ